



27

## 28 **1. Introduction**

29 Quantifying the rates and duration of deformation processes is key to understand how the  
30 continental crust deforms. Quite a lot is known about rates and duration of ductile deformation in the  
31 lower crust, for instance that shear zones can be active for 10s or 100s My (Schneider et al., 2013;  
32 Mottram et al., 2015). However, less is known about the duration and rates of folding processes in the  
33 upper crust. Short-term folding rates are usually captured by studying deformed terraces and alluvial fan  
34 ridges associated with active folds, and the dating of the inception and lifetime of folds is based on the  
35 extrapolation of these short-term rates back in time assuming a steady deformation rate.

36 The other classical mean to constrain the age and rate of upper crustal folding consists of dating  
37 growth strata. In orogenic forelands, contractional deformation causes folding of the pre-deformational  
38 sedimentary sequence and when sedimentation occurs continuously during deformation, growth strata  
39 are deposited synchronously with folding. Growth strata often show a characteristic pattern, such as  
40 decreasing dips up section toward the limbs of the fold, fan-like geometry and unconformities (Riba,  
41 1976; Fig.1). Several factors control growth strata patterns, such as kink-band migration, fold uplift,  
42 limb rotation and lengthening rates, as well as sedimentation and erosion rates (Suppe et al., 1992; Storti  
43 and Poblet, 1997). Chronostratigraphic constraints are critical for defining the duration and rate of fold  
44 growth (Butler and Lickorish, 1997). Dating the base of the growth strata defines the youngest initiation  
45 age for the fold, while post-growth strata conceal the final geometry of the fold and mark the end of  
46 folding (Fig.1).

47 However, preserved growth strata are not ubiquitous/are rare, and the folded multilayer typically  
48 includes only pre-growth strata. Also, the fold growth may be highly discontinuous through time,  
49 deformation being episodic at all timescales with tectonic uplift pulses of different duration and intensity  
50 interrupted by periods of variable extent in which no fold growth occurred (Masferro et al., 2002;  
51 Carrigan et al., 2016; Anastasio et al., 2018). Where available, the study of syntectonic unconformities  
52 (Barnes, 1996) or terraces (Mueller and Suppe, 1997) otherwise suggest that the growth of some folds  
53 may be caused by earthquake-related slip on active faults, which is by essence discontinuous. These  
54 studies emphasize the difficulty to extrapolate fold growth rates back in time. The age of fold initiation

55 obtained by assuming steady shortening rate, deposition rate and fold growth rate is therefore at best  
56 strongly biased, at worst false, so the duration of fold growth remains poorly constrained.

57         Folded sedimentary layers usually exhibit brittle mesostructures such as faults, joints and veins,  
58 and stylolites (e.g. Tavani et al., 2015, and references therein). These mesostructures accommodate the  
59 internal strain of strata during folding, but also before strata started to be tilted and after tilting, i.e.,  
60 when shortening can no longer be accommodated by fold growth (Fig.1). Several deformation stages  
61 can typically be identified in folded pre-compressional strata, starting with pre-shortening extension  
62 related to foreland flexure and bulging, followed by layer-parallel shortening (LPS, horizontal  
63 shortening of flat-lying strata) (Amrouch et al., 2010a; Callot et al., 2010; Lacombe et al., 2011; Tavani  
64 et al., 2006, 2008, 2011, 2012; Rocher et al., 2000; Beaudoin et al., 2012, 2016; Branellec et al., 2015).  
65 Continuing horizontal stress loading and shortening usually leads to folding, associated with strata tilting  
66 and curvature which are accommodated by flexural slip in the fold limbs and tangential longitudinal  
67 strain (outer arc extension and inner arc compression) at the fold hinge. The fold ‘locks’ when limb  
68 rotation and/or kink-band migration cannot accommodate shortening anymore. At that stage, strata  
69 tilting is over but continuous horizontal shortening leads to late stage fold tightening (LSFT),  
70 accommodated by late mesostructures developing irrespective of bedding dip (Fig. 1) (Amrouch et al.,  
71 2010a; Tavani et al., 2015).

72         Despite recent efforts (Wang et al., 2016; Grobe et al., 2019; Curzi et al., 2020; Cruset et al.,  
73 2020, 2021), the dating of the early-, syn- and late-folding mesostructures has received poor attention,  
74 although it is key to constrain not only the absolute timing of folding in the absence of growth strata,  
75 but also the entire duration of the fold-related contractional stages and the associated stress evolution  
76 from build-up to release. We explore hereinafter the possibility to define the age and duration of folding  
77 by investigating how and for how long pre-folding strata have been accommodating shortening from the  
78 onset to the end of the horizontal contraction from which the fold originated, an event we define as the  
79 folding event (Fig. 1). This approach will help better constrain the duration of fold growth, by dating  
80 directly the syn-folding mesostructures but also by bracketing the timing of fold growth through dating  
81 of the mesostructures that immediately predate and postdate strata tilting. Doing so will also enable to

82 capture the duration of the LPS and LSFT. These two deformation stages have been overlooked since  
83 they accommodate much less shortening than folding itself. However, they correspond to key periods  
84 of time for large scale fluid flow and related ore deposition in fold-and-thrust belts and sedimentary  
85 basins (e.g., Roure et al., 2005; Evans and Fischer, 2012; Beaudoin et al., 2014). For this purpose, we  
86 consider four natural folds for which we either compile existing data or provide new estimates of the  
87 age of LPS, fold growth and LSFT. Three of our examples are from fold-and-thrust belts (Apennines,  
88 Pyrenees), and one from the Laramide basement-cored folding province (Rocky Mountains). We show  
89 that mesostructures can be used to constrain the timing and duration of fold growth and/or of shortening  
90 preceding and following folding. Our results not only provide new estimates of the duration of folding,  
91 but also establish that the overall duration of the folding event may strongly vary as a function of the  
92 tectonic style of deformation. Beyond regional implications, this study paves the way to a better  
93 mechanical appraisal of contractional deformation and stress evolution in folded domains.

94

## 95 **2. Methods for dating the folding event using mesostructures**

96 In this paper, we focus on easily recognizable mesostructures that develop in the same  
97 contractional stage and under the same regional trend of horizontal shortening than folding. We report  
98 neither on microstructures such as calcite twins (Craddock et al., 1993; Lacombe et al., 2007, 2009;  
99 Rocher et al., 1996; Hnat et al., 2011; see review by Lacombe, 2010) nor on rock physical properties  
100 such as anisotropy of magnetic susceptibility (e.g, Aubourg et al., 2010; Amrouch et al., 2010b;  
101 Branellec et al., 2015, Weil and Yonkee, 2012). The main reason is that even both of them have been  
102 shown to be suitable recorders of the stress and strain history of folded strata (Lacombe et al., 2012),  
103 their precise dating remains to date out of reach.

104 In the four folds that we investigated, the sequence and age of mesostructures were established  
105 by various dating approaches, of which methodologies are briefly recalled below (Fig.2). Note that strata  
106 from which mesostructures were dated are mainly pre-folding strata, and that there have been few (if  
107 any) attempts at directly dating mesostructures that developed within growth strata. The reason is that  
108 the often poorly indurated syn-folding formations are less prone to fracturing and calcite cementation at

109 the time of deformation compared to pre-folding, well-indurated formations, which is evidenced by the  
110 paucity of fracture studies in syn-tectonic strata (e.g., Shackleton et al., 2011).

### 111 *2.1 Sequence of mesostructures related to the fold history*

112 The characterization of the sequence of deformation was based on field measurements of  
113 stylolites, faults, joints and veins, and their grouping into sets according to their statistical orientation,  
114 deformation mode and relative chronology established from abutting and crosscutting relationships  
115 (Fig.2A). Their timing with respect to fold growth (i.e., early, syn-, and late folding mesostructures) was  
116 further established by considering their current and unfolded attitude at fold hinge and limbs (eg.,  
117 Beaudoin et al, 2012, 2016; Tavani et al., 2015) (Fig.1).

118 Field observations (eg., Bellahsen et al., 2006; Ahmadhadi et al., 2008; Tavani et al., 2015) and  
119 numerical modelling (Guiton et al., 2003; Sassi et al., 2012) have emphasized the widespread  
120 reactivation during folding of joints and veins formed during pre-folding stages. The role of reactivation  
121 should not be, and has not been, overlooked in our study; however, for the sake of reliable absolute  
122 dating we focused on faults and veins the characteristics of which support that they newly formed at  
123 each deformation stage and show neither textural nor petrographic evidence of multiple opening or  
124 shearing events, should it be at the meso-scale or at the micro-scale.

125

### 126 *2.2 Dating veins and faults*

127 Calcite-bearing veins and faults (Fig.2A) can be dated by combining the absolute precipitation  
128 temperature of the fluids from which calcite cements formed as given by carbonate clumped isotope  $\Delta_{47}$   
129 thermometry with the burial-time history of strata (Fig.2B,D). Provided that (1) cementation was nearly  
130 coeval with fracturing, (2) the geotherm can be reliably estimated and (3) stable isotope geochemistry  
131 points towards fluid precipitation at thermal equilibrium with the host rock, clumped isotope  
132 thermometry of cements combined to strata burial history yields the absolute timing of the successive  
133 vein sets, hence the timing of the related deformation stages (Fig.2D) (Labeur et al., 2021).

134 Calcite cements can also be directly dated by carbonate geochronology (Fig.2B). Laser ablation–  
135 inductively coupled plasma–mass spectrometry (LA-ICP-MS) U-Pb dating of calcite consistently

136 reveals the age of brittle deformation events (Roberts and Walker, 2016; Nuriel et al., 2017; Hansman  
137 et al., 2018; Beaudoin et al., 2018; Roberts et al., 2020)(Fig.2B,D), provided that cementation was coeval  
138 with fracturing and that no later fluid infiltration and/or calcite recrystallization occurred (Roberts et al.,  
139 2021).

140

### 141 *2.3 Combining sedimentary stylolite roughness inversion for paleodepth and burial history to* 142 *constrain the onset of LPS*

143

144 The onset of LPS corresponds to the time at which the maximum principal stress  $\sigma_1$  switched  
145 from a vertical attitude related to compaction and/or to foreland flexural extension to a horizontal  
146 attitude in response to tectonic contraction (Beaudoin et al., 2020a). In order to constrain the timing of  
147 this switch, our approach relies on the capability of bedding-parallel, sedimentary stylolite (Fig.2A) to  
148 fossilize the magnitude of the vertical stress  $\sigma_1$  at the time dissolution stopped. Indeed, signal analysis  
149 (e.g. wavelets) of the final roughness of a sedimentary stylolite returns scale-dependent power laws, of  
150 which the transition length (crossover length  $L_c$ ) scales with the magnitude of the vertical stress  $\sigma_1$   
151 (Schmittbuhl et al, 2004; Toussaint et al., 2018) (Fig.2C). By analyzing a population of sedimentary  
152 stylolites with this inversion technique which has been validated by numerous studies (Ebner et al.,  
153 2009; Rolland et al., 2014; Bertotti et al., 2017; Beaudoin et al., 2016, 2019, 2020a,b), one can estimate  
154 the maximum burial depth at which pressure solution was active, with 12% uncertainty (Rolland et al.,  
155 2014). Combining this depth with the burial-time evolution of the strata as derived from well data and/or  
156 exposed stratigraphic successions reveals the time at which compaction-driven pressure solution halted  
157 in the rock because of the switch from a vertical to a horizontal  $\sigma_1$ , and thus the age of the onset of LPS  
158 (Fig. 2D). The validity of such an approach has been established on the basis of the comparison of the  
159 age of the onset of LPS determined this way with the oldest U-Pb absolute age of LPS-related veins  
160 (Beaudoin et al., 2020a).

161

## 162 **3. Dating natural folding events**

163 *3.1 Cingoli and San Vicino Anticlines (Apennines)*

164 The San Vicino and Cingoli anticlines belong to the Umbria-Marche Apennine Ridge (UMAR,  
165 Fig. 3A). Apenninic deformation occurred by the Tortonian in the west of UMAR to the late Messinian-  
166 early Pliocene in the east, reaching the Adriatic domain in the late Pliocene-Pleistocene (Calamita et al.,  
167 1994). UMAR undergoes post-orogenic extension since ~3 Ma, being younger eastward and marked by  
168 recent or active normal faults cutting through the nappe stack (Barchi, 2010). The San Vicino and the  
169 Cingoli anticlines involve platform carbonates overlain by a hemipelagic succession detached above  
170 Triassic evaporites. The folds formed in late Messinian-early Pliocene (~6-5 Ma) as indicated by growth  
171 strata preserved in the nearby Aliforni syncline (Fig.3B), following a period of foreland flexure-related  
172 extension marked by pre-contractinal normal faults associated with turbidite deposition lasting until  
173 early Messinian (~6.5 Ma) (Calamita et al., 1994; Mazzoli et al., 2002).

174 Field analysis in the Cingoli and San Vicino fault-bend anticlines (Fig.3B) has revealed three  
175 main sets of mesostructures (Beaudoin et al., 2020b; Labeur et al., 2021). Set I consists of vertical veins  
176 perpendicular to both bedding and fold axis and striking NE-SW, associated with bed-perpendicular  
177 tectonic stylolites with peaks trending NE-SW and plunging parallel to bedding dip which, after  
178 unfolding, indicates NE-SW-directed LPS. Set II veins are bed-perpendicular and strike NW-SE,  
179 parallel to the fold axis; they abut or cut across set I veins and formed in response to outer-arc extension  
180 at fold hinge. Set III comprises NE-SW striking veins closely associated with tectonic stylolites with  
181 horizontal peaks trending NE-SW - both veins and tectonic stylolites being vertical regardless of the  
182 bedding dip - and with conjugate vertical strike-slip faults which formed during a post-tilting horizontal  
183 NE-SW contraction, i.e., LSFT (Fig.3C).

184 Labeur et al (2021) focused on the Cingoli anticline to reconstruct the burial history of the early  
185 Cretaceous Maiolica Fm. and the Paleocene Scaglia Rossa Fm. The authors carried out an extensive  
186 inversion of the roughness of sedimentary stylolites from these formations to constrain the maximum  
187 depth at which compaction-related dissolution was active. The results are shown in Fig.3D, together  
188 with the timing of veins from sets I and II as deduced from  $\Delta_{47}$  thermometry (Labeur et al., 2021) by

189 considering a 23°C/km geotherm (Caricchi et al. 2015) and a 10°C surface temperature. The resulting  
190 timing for LPS, fold growth and LSFT is shown in Fig.3F.

191 To extend the published dataset to the San Vicino Anticline, veins from sets I, II and III were  
192 sampled in the Maiolica Fm. to perform U-Pb analyses for absolute dating. Selected veins display  
193 antitaxial, elongated-blocky or blocky textures (Bons et al., 2012) ensuring that the cements precipitated  
194 during, or soon after, vein opening. Cathodoluminescence observations further support the homogeneity  
195 of the cements (Fig.4) as well as the absence of any vein re-opening and calcite recrystallization or fluid  
196 infiltration that might cause anomalous younger (reset) ages (Roberts et al., 2021). U-Pb dating of calcite  
197 cements was conducted using LA-ICP-MS at the Institut des Sciences Analytiques et de Physico-Chimie  
198 pour l'Environnement et les Matériaux (IPREM) laboratory (Pau, France). Ages were determined from  
199 the total-Pb/U-Th algorithm of Vermeesch (2020), are quoted at 95% confidence, and include  
200 propagation of systematic uncertainties. Sample information, detailed methodology and results are  
201 provided in the Supplemental Material. Three veins from the San Vicino anticline yielded reliable ages:  
202  $6.1 \pm 2$  Ma for the set I vein,  $3.5 \pm 1$  Ma for the set II vein and  $3.7 \pm 0.3$  Ma for the set III vein (Fig. 3E).  
203 The large uncertainties on the U-Pb age from the set II vein lead to some overlap with the dates of set I  
204 and set III veins (Fig.3F). However, these veins have distinctive orientations, consistent relative  
205 chronology, and distinctive C and O stable isotopic signatures of their cements while being sampled in  
206 the same parts of the fold (Beaudoin et al., 2020b). These observations support that these veins were not  
207 cemented by the same fluid, hence were not cemented coevally. The absolute vein ages, combined with  
208 existing time constraints (Fig.3F), indicate that LPS occurred from ~6.5 to 5.5 Ma for both anticlines,  
209 followed by fold growth between ~5.5 and ~3.5 Ma, with a seemingly slightly longer duration in Cingoli  
210 than in San Vicino. LSFT started ~5 Ma in the Camerino syncline (Beaudoin et al., 2020b), ~4.5 Ma in  
211 San Vicino and ~3 Ma in Cingoli, and possibly lasted until the onset of post-orogenic extension in  
212 eastern UMAR (~2.5-2 Ma, Fig.3F). The entire folding event was thus very short, having lasted 3-4 My  
213 considering both anticlines as a whole (Fig.3F).

214 *3.2 Pico del Aguila Anticline (Pyrenees)*

215           The Pico del Aguila is a N160°E trending anticline in the southern Pyrenees (Fig. 5A), markedly  
216 oblique to the south Pyrenean thrust front. It formed in response to Pyrenean thrusting and detachment  
217 folding above Triassic evaporites (Poblet and Hardy, 1995; Vidal Royo et al., 2009, Fig. 5B). Growth  
218 strata (Fig.5B) indicate that the fold developed by late Lutetian-Priabonian (~ 42-35 Ma, Hogan and  
219 Burbank, 1996), before it was passively tilted and transported southward over the Guarga basement  
220 thrust (Jolivet et al., 2007).

221           Beaudoin et al. (2015) investigated the fracturing history of the Pico del Aguila (Fig. 5C). Three  
222 sets of bed-perpendicular joints/veins, oriented N080°E, N060°E and N045°E (from the oldest to the  
223 youngest as established from abutting/cross cutting relationships), were recognized. These three sets  
224 formed in progressively younging strata in response to a NE-SW-directed shortening while the area was  
225 undergoing a vertical axis 30-40° clockwise rotation (Fig.5C). This rotation agrees with the Bartonian-  
226 Priabonian clockwise rotation of 15-50° around a vertical axis identified from paleomagnetism (Pueyo  
227 et al., 2002). The field study also revealed bed-perpendicular joints oriented N160°E and N-S trending  
228 normal faults which formed during fold growth in response to outer-arc extension at fold hinge (Fig.5C).  
229 The end of the fold-related fracturing history (LSFT) is marked by the formation of N-S trending reverse  
230 faults and by the transpressional reactivation of earlier ENE striking joints under an E-W compression  
231 resulting from the local rotation of the regional NE-SW compression (Beaudoin et al., 2015). Post-  
232 folding, E-W trending reverse faults ultimately developed under the same N-S compression as the  
233 Guarga thrust (Fig.5C).

234           U-Pb dating of calcite cements reveals that the veins related to NE-SW directed LPS formed as  
235 early as  $\sim 61 \pm 3$  Ma ago, while late oblique-slip reverse faults (LSFT) and post-folding E-W reverse  
236 faults were dated  $19 \pm 5$  Ma and  $18-14 \pm 3$  Ma, respectively (Hoareau et al., 2021). LPS, folding and  
237 LSFT therefore lasted  $\sim 19$  My (61-42 Ma),  $\sim 7$  My (42-35 Ma) and  $\sim 17$  My (35-18 Ma), respectively  
238 (Fig.5D).

239

240    3.3 Sheep Mountain Anticline (Rocky Mountains)

241 The Sheep Mountain anticline is a thrust-related, basement-cored NW-SE striking fold that  
242 developed in the Bighorn basin (Figs. 6A and B) during the late Cretaceous-Paleogene Laramide  
243 contraction. Three main joint/vein sets were recognized there (Fig. 6C, Bellahsen et al., 2006; Amrouch  
244 et al., 2010; Barbier et al., 2012). Set I consists of bed-perpendicular, WNW-ESE oriented veins  
245 associated with tectonic stylolites with ~WNW-ESE horizontal peaks (after unfolding) (Amrouch et al.,  
246 2010a, 2011). This set formed prior to folding under a horizontal  $\sigma_1$  trending WNW-ESE, likely  
247 transmitted from the distant thin-skinned Sevier orogen at the time the Bighorn basin was still part of  
248 the Sevier undeformed foreland. Set II comprises vertical, bed-perpendicular joints/veins striking NE-  
249 SW, i.e., perpendicular to the fold axis. These veins are associated with tectonic stylolites with horizontal  
250 peaks oriented NE-SW and witness a NE-SW directed LPS (Varga, 1993; Amrouch et al., 2010a; Weil  
251 and Yonkee, 2012). The joints/veins of set III are bed-perpendicular and abut or cut across the veins of  
252 the former sets. They strike NW-SE, i.e., parallel to the fold axis, and their distribution mainly at the  
253 hinge zone of the fold support their development in response to outer-arc extension at the hinge of the  
254 growing anticline (Fig.6C). Widespread reverse and strike-slip faults also formed during LPS and LSFT,  
255 while bedding-parallel slip surfaces developed during fold growth (Amrouch et al., 2010a).

256 Veins from sets I, II and III were dated by means of U-Pb (Beaudoin et al., 2018). Set I veins  
257 yielded ages between 81 and 72 Ma, supporting their pre-Laramide formation. The Laramide LPS-  
258 related veins were dated 72–50 Ma. The age of set III veins constrains the timing of folding in the  
259 absence of preserved growth strata to 50–35 Ma (Beaudoin et al., 2018). Laramide LPS and fold growth  
260 therefore lasted ~20-25 My and ~15 My, respectively (Fig. 6D). The duration of the LSFT is poorly  
261 constrained, being bracketed between 35 Ma and the onset of the Basin and Range extension and  
262 Yellowstone hot-spot activity at ~17 Ma (Camp et al., 2015, Fig. 6D).

#### 263 **4. Discussion and conclusion**

264 The absolute dating of mesostructures definitely confirms the sequence of deformation usually  
265 deduced from orientation data and relative chronology with respect to bedding attitude, which includes  
266 LPS, fold growth (e.g., strata tilting) and LSFT (Fig.1). This sequence is valid for the four folds studied,  
267 despite the San Vicino, Cingoli and Pico del Aguila anticlines developed above a decollement in a fold-

268 and-thrust belt while the Sheep Mountain anticline formed as a basement-cored forced fold above a  
269 basement thrust. The overall consistency between the ages of growth strata when preserved, the time  
270 constraints derived from our multi-proxy analysis coupling isotopic geochemistry of cements and  
271 stylolite paleopiezometry, and the U-Pb ages on early-, syn- and late-folding mesostructures  
272 demonstrates the reliability of our approach. Minor age overlaps are observed only when the duration  
273 of each deformation stage was shorter than age uncertainties, i.e., in the case of recent and rapid  
274 deformation (San Vicino and Cingoli, Fig.3F). Note that age overlaps could also relate with the fact that  
275 LPS and fold growth may slightly overlap, as documented in the Sibillini thrust anticline, i.e., the  
276 southern continuation of the San Vicino anticline (Tavani et al., 2012).

277 In the four investigated anticlines, fold growth lasted between 1.5 Ma and 15 Ma, in accordance  
278 with previous estimates of fold growth duration elsewhere using either syntectonic sedimentation (Holl  
279 and Anastasio, 1993; Anastasio et al., 2018) or mechanical modeling (Yamato et al., 2011). Moreover,  
280 our study quantifies for the first time the duration of the contraction before and after fold growth. The  
281 results unexpectedly reveal that LPS and LSFT, which accommodate lower amounts of shortening than  
282 fold growth but which are associated with substantial - if not most of - small-scale rock damage, may  
283 have lasted much longer than fold growth itself. Such a trend could be key for the understanding of the  
284 history of foreland basins, including mechanical evolution of strata and past fluid flow dynamics (Roure  
285 et al., 2005; Beaudoin et al., 2014).

286 Dating precisely the onset of LPS, whatever the technique used (U-Pb geochronology or  
287 absolute thermometry of calcite cements of mesostructures) is difficult because the entire range of vein  
288 ages may not be captured with certainty due to limited sampling. However, the onset of LPS can be  
289 further constrained either by the sedimentary record of the foreland flexure preceding contraction (San  
290 Vicino) or by the estimate of the time at which compaction-related pressure solution along sedimentary  
291 stylolites halted in the rocks in response to the switch of  $\sigma_1$  axis from vertical to horizontal (Cingoli).  
292 The end of LSFT is also difficult to constrain precisely, but an upper bound is given by the change from  
293 fold-related shortening to a new regional state of stress. The latter is illustrated by the onset of post-

294 orogenic extension in eastern UMAR (Fig.3), by the late Pyrenean compression in the Pico del Aguila  
295 area (Fig. 5) and by the Basin and Range extension in the Laramide province (Fig.6).

296         The four examples of folds also show that the overall duration of the folding event is variable  
297 (Fig.7). Fold growth lasted longer in the case of forced folding above a high angle basement thrust  
298 (Sheep Mountain) compared to fault-bend folding (San Vicino and Cingoli) along a flat-ramp  
299 decollement and detachment folding (Pico del Aguila) above a weak detachment layer in the cover (Fig.  
300 7). The rapid fold growth and the relatively short LSFT in San Vicino and Cingoli are in line with the  
301 high rates of contraction and migration of deformation in the Apennines (Calamita et al., 1994, Fig .7).  
302 In contrast, LSFT appears to last longer when folding is anchored to a high angle basement thrust or  
303 when the fold is located at the front of the orogenic wedge, i.e., when the later propagation of  
304 deformation is limited or slow or when it occurs in a complex sequence (Pico del Aguila and Sheep  
305 Mountain, Fig.7). The duration of LPS reflects to some degree the duration of the stress/strain  
306 accumulation in rocks required to generate folding, which can depend on the structural style (Beaudoin  
307 et al., 2020c). Our results support that a longer LPS (and a higher level of differential stress as well) is  
308 required to cause the inversion of a high angle basement normal fault and related forced folding of the  
309 undetached sedimentary cover (Sheep Mountain) than to initiate folding of the cover above a weak  
310 decollement (Pico del Aguila, Cingoli and San Vicino, Fig. 7). The longer LPS at Pico del Aguila with  
311 respect to San Vicino and Cingoli (Fig.7) likely reflects the longer accumulation of displacement  
312 required to initiate folding oblique to the regional compression rather than perpendicular to it. It is worth  
313 to note that at first glance the fracture pattern (eg, Tavani et al., 2015) remains basically similar whatever  
314 the overall duration of the folding event and related deformation stages.

315         In summary, beyond regional implications, this study demonstrates that pre-, syn- and post-  
316 tilting mesostructures that formed under the same contraction as folding can be successfully dated. Our  
317 results bring for the first time absolute time constraints on the age and duration on the entire folding  
318 event for several upper crustal folds formed in different contractional settings. In particular, we not only  
319 better constrain the age and duration of the fold growth stage, but also the onset and duration of the  
320 layer-parallel shortening stage that predates folding, and the duration and end of the late stage fold

321 tightening. Because the duration of each deformation stage is found to depend on the structural style  
322 and/or the regional sequence of deformation, our results emphasize the need to more carefully consider  
323 the entire folding event for a better appraisal of folding processes and stress/strain evolution in orogenic  
324 forelands, and for a more accurate prediction of host rock damage and fluid migrations in naturally  
325 fractured reservoirs within folded domains.

326

### 327 **Acknowledgements**

328 NB is funded through the ISITE program E2S, supported by ANR PIA and Region Nouvelle- Aquitaine.  
329 The authors would like to thank the two anonymous reviewers for their constructive comments, as well  
330 as Fabrizio Storti, Catherine Mottram and Stephen Marshak for their comments on an earlier version of  
331 the manuscript. The authors also thank Topical Editor Virginia Toy for editorial handling.

332

### 333 **Figure captions**

334 Fig.1. Concept of folding event and associated mesostructures and growth strata.

335 Fig.2. Principle of dating of mesostructures related to the folding event. A. Photograph of a bedding-  
336 parallel sedimentary stylolite cut by a vertical vein related to layer-parallel shortening (LPS). B.  
337 Principle of dating calcite veins using LA-ICP-MS, with laser ablation spots and final Tera-Wasserburg  
338 diagram. C. Principle of inversion of the roughness of sedimentary stylolites for stress.  $\sigma_v$  is the vertical  
339 stress,  $\alpha = \frac{(1-2\nu)*(1+\nu)^2}{30\pi(1-\nu)^2}$ ,  $\gamma$  is the solid-fluid interfacial energy,  $\nu$  is the Poisson ratio, E is the Young  
340 modulus,  $\rho$  is the dry density, g is the gravitational field acceleration and z is the depth. D. Principle of  
341 the combination of U-Pb dating and absolute  $\Delta_{47}$  thermometry of calcite cements (here for LPS-related  
342 veins) with maximum depth of burial-related dissolution inferred from roughness inversion of  
343 sedimentary stylolites and burial-time evolution of strata to derive the timing of deformation stages  
344 during the folding event. Regional data are from Mazzoli et al., 2002 (flexure), Calamita et al. 1994  
345 (folding and thrusting), Beaudoin et al., 2020b (LSFT).

346

347 Fig.3. San Vicino and Cingoli anticlines: A: location (AS: Adriatic Sea; TS: Tyrrhenian Sea). B: Cross  
348 section (after Mazzoli et al., 2002). C: Orientation of the main sets of mesostructures (relative  
349 chronology, 1 to 3), reported in current or unfolded attitude on a lower hemisphere Schmidt stereonet,  
350 and associated paleostress evolution. \* denotes mesostructures dated using U-Pb. D: Burial model of  
351 Cingoli constructed considering thickness from stratigraphic and well data corrected for chemical and  
352 physical compaction (modified from Labeur et al., 2021). The range of depths reconstructed from  
353 sedimentary stylolite roughness inversion (with uncertainty shaded in light grey) are reported for each  
354 formation as grey levels. The results of clumped isotope analysis (i.e., temperatures of precipitation of  
355 vein cements at thermal equilibrium with the host rock) are reported for LPS-related veins (blue) and  
356 syn-folding veins (red). The deduced timing of the deformation stages is reported. E: Age dating results  
357 for veins from San Vicino anticline: Tera-Wasserburg concordia plots for carbonate samples showing  
358  $^{238}\text{U}/^{206}\text{Pb}$  vs  $^{207}\text{Pb}/^{206}\text{Pb}$  for veins of sets I (LPS-related) and III (LSFT-related)(n—no. of spots).  
359 MSWD—mean square of weighted deviates. F: Timing and duration of deformation stages. Color code  
360 for C and F: dark blue: flexure-related extension. blue: layer-parallel shortening (LPS); red: fold growth;  
361 green: late stage fold tightening (LSFT); yellow: post-folding extension.

362

363 Fig.4. 2D scans of veins dated by LA-ICP-MS U-Pb geochronology from San Vicino anticline, with  
364 location of the ablation spots and diagenetic state observed under cathodoluminescence microscopy. A:  
365 sample A16 (LPS-related vein). B: sample A19 (syn-folding vein). C: sample A20 (LSFT-related vein).

366

367 Fig.5. Pico del Aguila anticline: A: location (AB: Aquitaine Basin, JB: Jaca Basin, EB: Ebro Basin,  
368 PAZ: Pyrenean Axial Zone; P: Paleozoic; M: Mesozoic; C: Cenozoic). B: Cross sections (north after  
369 Poblet et al., 1997, south after Beaudoin et al., 2015). C: Orientation of the main sets of mesostructures  
370 (relative chronology, 1 to 5), reported in current or unfolded attitude on a lower hemisphere Schmidt  
371 stereonet (same key as Fig.3), and associated structural and paleostress evolution. Block diagrams  
372 modified after Beaudoin et al. (2015). \* denotes mesostructures dated using U-Pb. D: Timing and

373 duration of deformation stages. Color code for C and D : blue: layer-parallel shortening (LPS); red: fold  
374 growth; green: late stage fold tightening (LSFT); yellow: post-folding compression.

375

376 Fig.6. Sheep Mountain anticline: A: location (BHB: Bighorn Basin; WRB: Wind River Basin; PRB:  
377 Powder River Basin; GGB: Greater Green River Basin; DB: Denver Basin). B: Cross section (after  
378 Amrouch et al., 2010); C: Orientation of the main sets of veins (relative chronology, 1 to 3), shown on  
379 a field photograph and on a block-diagram of the final fold geometry, reported in unfolded attitude on a  
380 lower hemisphere Schmidt stereonet (same key as Fig.3), and associated structural and paleostress  
381 evolution. \* denotes mesostructures dated using U-Pb. D: Timing and duration of the deformation  
382 stages. Color code for C and D: grey: pre-folding layer-parallel shortening kinematically unrelated to  
383 folding; blue: layer-parallel shortening (LPS); red: fold growth; green: late stage fold tightening (LSFT);  
384 yellow: post-folding extension.

385 Fig.7. Compared durations of the deformation stages of the folding event, fold style (= final fold  
386 geometry) and sequence of regional deformation for the four studied folds (circled numbers 1 to 6 :  
387 order of structural development, i.e., sequence of folding/thrusting, with corresponding ages in Ma  
388 (between parentheses), red : from this study; black : from the literature (Beaudoin et al., 2018 for  
389 Wyoming, Jolivet et al., 2007 for the Pyrenees, Calamita et al., 1994 and Curzi et al., 2020 for the  
390 Apennines). Color code: blue: layer-parallel shortening (LPS); red: fold growth; green: late stage fold  
391 tightening (LSFT); yellow: post-folding extension/compression.

392

### 393 **References**

394

- 395 Ahmadhadi, F., Daniel, J.M., Azzizadeh, M., Lacombe, O.: Evidence for pre-folding vein development  
396 in the Oligo-Miocene Asmari Formation in the Central Zagros Fold Belt, Iran, *Tectonics*, 27, 2008.
- 397 Amrouch, K., Lacombe, O., Bellahsen, N., Daniel, J. M., Callot, J. P.: Stress and strain patterns,  
398 kinematics and deformation mechanisms in a basement-cored anticline: Sheep Mountain Anticline,  
399 Wyoming, *Tectonics*, 29(1), TC1005, 2010a.
- 400 Amrouch, K., Robion, P., Callot, J. P., Lacombe, O., Daniel, J. M., Bellahsen, N., Faure, J. L.: Constraints  
401 on deformation mechanisms during folding provided by rock physical properties: a case study at Sheep  
402 Mountain anticline (Wyoming, USA), *Geophysical Journal International*, 182(3), 1105-1123, 2010b.

403 Amrouch, K., Beaudoin, N., Lacombe, O., Bellahsen, N., Daniel, J.M.: Paleostress magnitudes in folded  
404 sedimentary rocks, *Geophysical Research Letters*, 38, L17301, 2011.

405 Anastasio, D., Kodama, K., Parés, J.: Episodic deformation rates recovered from growth strata, Pyrenees,  
406 *Search and Discovery Article*, 30553, 2018.

407 Aubourg, C., Smith, B., Eshraghi, A., Lacombe, O., Authemayou, C., Amrouch, K., Bellier O.,  
408 Mouthereau, F.: New magnetic fabric data and their comparison with palaeostress markers in the  
409 Western Fars Arc (Zagros, Iran): tectonic implications, *Geological Society London Special Publications*,  
410 330(1), 97-120, 2010.

411 Barbier, M., Leprêtre, R., Callot, J. P., Gasparini, M., Daniel, J. M., Hamon, Y., Lacombe O., Floquet,  
412 M.: Impact of fracture stratigraphy on the paleo-hydrogeology of the Madison Limestone in two  
413 basement-involved folds in the Bighorn basin,(Wyoming, USA). *Tectonophysics*, 576, 116-132, 2012.

414 Barchi, M.: The Neogene–Quaternary evolution of the Northern Apennines: crustal structure, style of  
415 deformation and seismicity, *Journal of Virtual Explorer*, 36, 2010.

416 Barnes P.M.: Active folding of Pleistocene unconformities on the edge of the Australian-Pacific plate  
417 boundary zone, offshore North Canterbury, New Zealand, *Tectonics*, 15, 623-640, 1996.

418 Beaudoin, N., Leprêtre, R., Bellahsen, N., Lacombe, O., Amrouch, K., Callot, J.P., Emmanuel, L., Daniel,  
419 J.M.: Structural and microstructural evolution of the Rattlesnake Mountain Anticline (Wyoming, USA):  
420 New insights into the Sevier and Laramide orogenic stress build-up in the Bighorn Basin,  
421 *Tectonophysics*, 576-577, 20–45, 2012.

422 Beaudoin, N., Koehn, D., Lacombe, O., Lecouty, A., Billi, A., Aharonov, E., Parlangeau, C.:  
423 Fingerprinting stress: Stylolite and calcite twinning paleopiezometry revealing the complexity of  
424 progressive stress patterns during folding-The case of the Monte Nero anticline in the Apennines, Italy,  
425 *Tectonics*, 35, 1687-1712, 2016.

426 Beaudoin, N., Lacombe, O., Roberts, N. M. W., Koehn, D.: U-Pb dating of calcite veins reveals complex  
427 stress evolution and thrust sequence in the Bighorn Basin, Wyoming, USA, *Geology*, 46, 1015-1018,  
428 2018.

429 Beaudoin, N., Huyghe, D., Bellahsen, N., Lacombe, O., Emmanuel, L., Mouthereau, F., Ouahnon, L.:  
430 Fluid systems and fracture development during syn-depositional fold growth: example from the Pico del  
431 Aguila Anticline, Sierras Exteriores, Southern Pyrenees, Spain, *Journal of Structural Geology*, 70, 23-  
432 38, 2015.

433 Beaudoin, N., Lacombe, O., David, M.E., Koehn, D.: Does stress transmission in forelands depend on  
434 structural style? Distinctive stress magnitudes during Sevier thin-skinned and Laramide thick-skinned  
435 layer-parallel shortening in the Bighorn Basin (USA) revealed by stylolite and calcite twinning  
436 paleopiezometry, *Terra Nova*, 32, 225-233, 2020c.

437 Beaudoin, N., Labeur, A., Lacombe, O., Koehn, D., Billi, A., Hoareau, G., Boyce, A., John, C.M.,  
438 Marchegiano, M., Roberts, N.M., Millar, I.L., Claverie, F., Pecheyran, C., Callot, J.P.: Regional-scale  
439 paleofluid system across the Tuscan Nappe - Umbria Marche Apennine Ridge (northern Apennines) as  
440 revealed by mesostructural and isotopic analyses of stylolite-vein networks, *Solid Earth*, 11, 4, 1617-  
441 1641,2020b

442 Beaudoin, N., Bellahsen, N., Lacombe, O., Emmanuel, L., Pironon, J.: Crustal-scale fluid flow during the  
443 tectonic evolution of the Bighorn Basin (Wyoming, USA), *Basin Research*, 26(3), 403-435, 2014.

444 Beaudoin N. E., Lacombe, O., Koehn, D., David, M.E., Farrell, N., Healy, D.: Vertical stress history and  
445 paleoburial in foreland basins unravelled by stylolite roughness paleopiezometry: Insights from  
446 bedding-parallel stylolites in the Bighorn Basin,Wyoming, USA, *Journal of Structural Geology*. 136,  
447 104061, 2020a.

448 Bellahsen, N., Fiore, P., Pollard, D.D.: The role of fractures in the structural interpretation of Sheep  
449 Mountain Anticline, Wyoming, *Journal of Structural Geology*, 28, 850-867, 2006.

450 Bertotti, G., de Graaf, S., Bisdom, K., Oskam, B., Vonhof, H.B., Bezerra, F.H.R., Reijmer, J.J.G., Cazarin,  
451 C.L.: Fracturing and fluid-flow during post-rift subsidence in carbonates of the Jandaíra Formation,  
452 Potiguar Basin, NE Brazil, *Basin Research*, 29, 836-853, 2017.

453 Bons, P.D., Elburg, M.A., Gomez-Rivas, E.: A review of the formation of tectonic veins and their  
454 microstructures, *Journal of Structural Geology*, 43, 33–62, 2012.

455 Branellec, M., Callot, J. P., Nivière, B., Ringenbach, J. C.: The fracture network, a proxy for mesoscale  
456 deformation: Constraints on layer parallel shortening history from the Malargüe fold and thrust belt,  
457 Argentina, *Tectonics*, 34(4), 623-647, 2015.

458 Butler, R.W.H., Lickorish, W.H.: Using high-resolution stratigraphy to date fold and thrust activity:  
459 examples from the Neogene of south-central Sicily, *Journal of the Geological Society*, 154, 633–643,  
460 1997.

461 Calamita, F., Cello, G., Deiana, G., Paltrinieri, W.: Structural styles, chronology rates of deformation, and  
462 time-space relationships in the Umbria-Marche thrust system (central Apennines, Italy), *Tectonics*, 13,  
463 873-881, 1994.

464 Callot, J.P., Robion, P., Sassi, W., Guiton, M.L.E., Kallel, N., Daniel, J.M., Mengus, J.M., Schmitz, J.:  
465 Magnetic characterisation of folded aeolian sandstones: interpretation of magnetic fabric in diamagnetic  
466 rocks, *Tectonophysics*, 495, 230-245, 2010.

467 Camp V.E., Pierce K.L., Morgan L.A. : Yellowstone plume trigger for Basin and Range extension, and  
468 coeval emplacement of the Nevada–Columbia Basin magmatic belt, *Geosphere*, 1, 2; 203–225, 2015.

469 Caricchi, C., Aldega, L., Corrado, S. Reconstruction of maximum burial along the Northern Apennines  
470 thrust wedge (Italy) by indicators of thermal exposure and modeling, *Geological Society of America*  
471 *Bulletin*, 127, 428–442, 2015.

472 Carrigan, J.H., Anastasio D.J., Kodama K.P., Parés J.M.: Fault-related fold kinematics recorded by  
473 terrestrial growth strata, Sant Llorenç de Morunys, Pyrenees Mountains, NE Spain, *Journal of Structural*  
474 *Geology*, 91, 161-176, 2016.

475 Curzi, M., Aldega, L., Bernasconi, S. M., Berra, F., Billi, A., Boschi, C., Franchini S., Van der Lelij R,  
476 Viola G., Carminati, E.: Architecture and evolution of an extensionally-inverted thrust (Mt. Tancia  
477 Thrust, Central Apennines): Geological, structural, geochemical, and K–Ar geochronological  
478 constraints, *Journal of Structural Geology*, 136, 104059, 2020.

479 Craddock, J. P., Jackson, M., van der Pluijm, B. A., Versical, R. T.: Regional shortening fabrics in eastern  
480 North America: Far-field stress transmission from the Appalachian-Ouachita Orogenic Belt, *Tectonics*,  
481 12(1), 257-264, 1993.

482 Cruset, D., Vergés, J., Albert, R., Gerdes, A., Benedicto, A., Cantarero, I., & Travé, A.: Quantifying  
483 deformation processes in the SE Pyrenees using U–Pb dating of fracture-filling calcites, *Journal of the*  
484 *Geological Society*, 177(6), 1186-1196, 2020.

485 Cruset, D., Vergés, J., Rodrigues, N., Belenguer, J., Pascual-Cebrian, E., Almar, Y., Perez-Caceres I.,  
486 Macchiavelli C., Trave A., Beranoaguirre A., Albert R., Gerdes A., Messenger, G.: U–Pb dating of  
487 carbonate veins constraining timing of beef growth and oil generation within Vaca Muerta Formation  
488 and compression history in the Neuquén Basin along the Andean fold and thrust belt, *Marine and*  
489 *Petroleum Geology*, 132, 105204, 2021.

490 Ebner, M., Koehn, D., Toussaint, R., Renard, F., Schmittbuhl, J.: Stress sensitivity of stylolite  
491 morphology, *Earth and Planetary Science Letters*, 277, 394-398, 2009.

492 Evans, M. A., Fischer, M. P.: On the distribution of fluids in folds: A review of controlling factors and  
493 processes, *Journal of Structural Geology*, 44, 2-24, 2012.

494 Grobe, A., von Hagke, C., Littke, R., Dunkl, I., Wübbeler F., Muechez P., Urai JL: Tectono-thermal  
495 evolution of Oman's Mesozoic passive continental margin under the obducting Semail Ophiolite: a case  
496 study of Jebel Akhdar, Oman, *Solid Earth* 10 (1), 149-175, 2019.

497 Guiton M.L., Sassi W., Leroy Y., Gauthier B.D.: Mechanical constraints on the chronology of fracture  
498 activation in folded Devonian sandstones of the western Moroccan Anti-Atlas, *Journal of Structural*  
499 *Geology*, 25, 1317-1330, 2003.

500 Hansman, R.J., Albert, R., Gerdes, A., Ring, U.: Absolute ages of multiple generations of brittle structures  
501 by U-Pb dating of calcite, *Geology*, 46, 207-210, 2018.

502 Hnat, J. S., van der Pluijm, B. A.: Foreland signature of indenter tectonics: Insights from calcite twinning  
503 analysis in the Tennessee salient of the Southern Appalachians, USA, *Lithosphere*, 3(5), 317-327, 2011.

504 Hoareau, G., Crognier, N., Lacroix, B., Aubourg, C., Roberts, N.W., Niemi, N., Branellec, M., Beaudoin,  
505 N.E., Suárez Ruiz, I. : Combination of  $\Delta 47$  and U-Pb dating in tectonic calcite veins unravel the last  
506 pulses related to the Pyrenean Shortening (Spain), *Earth and Planetary Science Letters*, 553, 116636,  
507 2021.

508 Hogan, P.J., Burbank, D.W.: Evolution of the Jaca piggyback basin and emergence of the external Sierras,  
509 southern Pyrenees. In: Friend, P.F., Dabrio, C.J. (Eds.), *Tertiary Basins of Spain*. Cambridge Univ.  
510 Press, 153-160, 1996.

511 Holl, J. E., Anastasio, D. J.: Paleomagnetically derived folding rates, southern Pyrenees, Spain, *Geology*,  
512 21, 271-274, 1993.

513 Jolivet, M., Labaume, P., Monie, P., Brunel, M., Arnaud, N., Campani, M.: Thermochronology constraints  
514 for the propagation sequence of the south Pyrenean basement thrust system (France-Spain), *Tectonics*  
515 26, TC5007, 2007.

516 Labeur, A., Beaudoin, N.E., Lacombe, O., Emmanuel, L., Petracchini, L., Daëron, M., Klimowicz, S.,  
517 Callot, J.-P.: Burial-deformation history of folded rocks unraveled by fracture analysis, stylolite  
518 paleopiezometry and vein cement geochemistry: A case study in the Cingoli Anticline (Umbria-Marche,  
519 Northern Apennines), *Geosciences*, 11, 135, 2021.

520 Lacombe, O., Bellahsen, N., Mouthereau, F.: Fracture patterns in the Zagros Simply Folded Belt (Fars,  
521 Iran): constraints on early collisional tectonic history and role of basement faults, *Geological Magazine*,  
522 148(5-6), 940-963, 2011.

523 Lacombe, O., Amrouch, K., Mouthereau, F., Dissez, L.: Calcite twinning constraints on late Neogene  
524 stress patterns and deformation mechanisms in the active Zagros collision belt, *Geology*, 35, 263-266,  
525 2007.

526 Lacombe, O., Malandain, J., Vilasi, N., Amrouch, K., Roure, F.: From paleostresses to paleoburial in  
527 fold-thrust belts: preliminary results from calcite twin analysis in the Outer Albanides, *Tectonophysics*  
528 475, 128-141, 2009.

529 Lacombe, O.: Calcite twins, a tool for tectonic studies in thrust belts and stable orogenic forelands, *Oil &*  
530 *Gas Science and Technology-Revue d'IFP Energies nouvelles*, 65(6), 809-838, 2010.

531 Lacombe O., Tavani S., Soto R.: Into the deformation history of folded rocks, *Special Issue*,  
532 *Tectonophysics*, 576-577, 1-3, 2012.

533 Masferro, J. L., Bulnes, M., Poblet, J., Eberli, G. P.: Episodic folding inferred from syntectonic carbonate  
534 sedimentation: the Santaren anticline, Bahamas foreland, *Sedimentary Geology*, 146, 11-24, 2002.

535 Mazzoli, S., Deiana, G., Galdenzi, S., Cello, G.: Miocene fault-controlled sedimentation and thrust  
536 propagation in the previously faulted external zones of the Umbria-Marche Apennines, Italy, *EGU*  
537 *Stephan Mueller Special Publication Series*, 1, 195-209, 2002.

538 Mottram, C. M., Parrish, R. R., Regis, D., Warren, C. J., Argles, T. W., Harris, N. B., Roberts, N. M.:  
539 Using U-Th-Pb petrochronology to determine rates of ductile thrusting: Time windows into the Main  
540 Central Thrust, Sikkim Himalaya, *Tectonics*, 34(7), 1355-1374, 2015.

541 Mueller K. Suppe J.: Growth of Wheeler Ridge anticline, California: geomorphic evidence for fault-bend  
542 folding behavior during earthquakes, *Journal of structural geology*, 19, 383-396, 1997.

543 Nuriel P., Weinberger R., Kylander-Clark A.R.C., Hacker B.R., Craddock J.P.: The onset of the Dead  
544 Sea transform based on calcite age-strain analyses, *Geology* 45 (7), 587-590, 2017.

545 Poblet, J., McClay, K., Storti, F., Munoz, J.A.: Geometry of syntectonic sediments associated

546 with single-layer detachment folds, *Journal of Structural Geology*, 19, 369-381, 1997.

547 Poblet, J., Hardy, S.: Reverse modelling of detachment folds; application to the Pico del Aguila anticline  
548 in the south-central Pyrenees (Spain), *Journal of Structural Geology* 17, 1707-1724, 1995.

549 Pueyo, E.L., Millan, H., Pocoví, A.: Rotation velocity of a thrust: a paleomagnetic study in the External  
550 Sierras (Southern Pyrenees), *Sedimentary Geology*, 146, 191-208, 2002.

551 Riba, O.: Syntectonic unconformities of the Alto Cardener, Spanish Pyrenees: A genetic interpretation,  
552 *Sedimentary Geology*, 15, 213–233, 1976.

553 Roberts, N. M., Walker, R. J.: U-Pb geochronology of calcite-mineralized faults: Absolute timing of rift-  
554 related fault events on the northeast Atlantic margin, *Geology*, 44, 531-534, 2016.

555 Roberts, N. M. W., Drost, K., Horstwood, M. S. A., Condon, D. J., Chew, D., Drake, H., Milodowski, A.  
556 E., McLean, N. M., Smye, A. J., Walker, R. J., Haslam, R., Hodson, K., Imber, J., Beaudoin, N., Lee, J.  
557 K.: Laser ablation inductively coupled plasma mass spectrometry (LA-ICP-MS) U–Pb carbonate  
558 geochronology: strategies, progress, and limitations, *Geochronology*, 2, 33-61, 2020.

559 Roberts, N. M., Žák, J., Vacek, F., Sláma, J.: No more blind dates with calcite: Fluid-flow vs. fault-slip  
560 along the Očkov thrust, Prague Basin, *Geoscience Frontiers*, 12(4), 101143, 2021.

561 Rocher, M., Lacombe, O., Angelier, J., Chen H.W.: Mechanical twin sets in calcite as markers of recent  
562 collisional events in a fold-and-thrust belt: evidence from the reefal limestones of southwestern Taiwan,  
563 *Tectonics* 15, 984–996, 1996.

564 Rocher, M., Lacombe, O., Angelier, J., Deffontaines, B., Verdier, F.: Cenozoic folding and faulting in the  
565 south Aquitaine Basin (France): insights from combined structural and paleostress analyses, *Journal of*  
566 *Structural Geology*, 22, 627–645, 2000.

567 Rolland, A., Toussaint, R., Baud, P., Schmittbuhl, J., Conil, N., Koehn, D., Renard, F., Gratier, J.-P.:  
568 Modeling the growth of stylolites in sedimentary rocks, *Journal of Geophysical Research: Solid Earth*,  
569 117, B06403, 2012.

570 Roure, F., Swennen, R., Schneider, F., Faure, J.L., Ferket, H., Guilhaumou, N., Osadetz, K., Robion, P.,  
571 Vandeginste, V.: Incidence and Importance of Tectonics and Natural Fluid Migration on Reservoir  
572 Evolution in Foreland Fold-And-Thrust Belts, *Oil & Gas Science and Technology*, 60, 67–106, 2005.

573 Sassi, W., Guiton, M., Leroy, Y.M., Kallel, N., Callot, J.P., Daniel, J.M., Lerat, O., Faure, J.L.: Constraints  
574 on mechanical modelling of folding provided by matrix deformation and fracture network analysis: The  
575 case of Split Mountain (Utah, USA), *Tectonophysics*, 576-577, 197-215, 2012.

576 Schmittbuhl, J., Renard, F., Gratier, J. P., Toussaint, R.: Roughness of stylolites: implications of 3D high  
577 resolution topography measurements, *Physical Review Letters*, 93, 238501, 2004.

578 Schneider, S., Hammerschmidt, K., Rosenberg, C. L.: Dating the longevity of ductile shear zones: Insight  
579 from  $^{40}\text{Ar}/^{39}\text{Ar}$  in situ analyses, *Earth and Planetary Science Letters*, 369, 43-58, 2013.

580 Shackleton, J. R., Cooke, M. L., Verges, J., Sima, T.: Temporal constraints on fracturing associated with  
581 fault-related folding at Sant Corneli anticline, Spanish Pyrenees, *Journal of Structural Geology*, 33(1),  
582 5-19, 2011.

583 Storti, F., Poblet, J.: Growth stratal architectures associated to decollement folds and fault-propagation  
584 folds. Inferences on fold kinematics, *Tectonophysics*, 282(1-4), 353-373, 1997.

585 Suppe, J., Chou, G.T. and Hook, S.C.: Rates of folding and faulting determined from growth strata. In:  
586 McClay, K.R. (Ed.), *Thrust Tectonics*. Chapman & Hall, Suffolk, pp.105-121, 1992.

587 Tavani, S., Storti, F., Lacombe, O., Corradetti, A., Muñoz, J., Mazzoli, S.: A review of deformation pattern  
588 templates in foreland basin systems and fold-and-thrust belts: Implications for the state of stress in the  
589 frontal regions of thrust wedges, *Earth-Science Reviews*, 141, 82-104, 2015.

590 Tavani S., Storti F., Fernández O, Muñoz JA, Salvini F.: 3-D deformation pattern analysis and evolution  
591 of the Añisclo anticline, southern Pyrenees, *Journal of Structural Geology*, 28 (4), 695-712, 2006.

592 Tavani S., Storti F., Salvini F., Toscano C. : Stratigraphic versus structural control on the deformation  
593 pattern associated with the evolution of the Mt. Catria anticline, Italy, *Journal of Structural Geology*, 30  
594 (5), 664-681, 2008.

595 Tavani S., Mencos J., Bausà J., Muñoz JA. : The fracture pattern of the Sant Corneli Bóixols oblique  
596 inversion anticline (Spanish Pyrenees), *Journal of Structural Geology* 33 (11), 1662-1680, 2011.

597 Tavani, S., Storti, F., Bausa, J., & Munoz, J. A.: Late thrusting extensional collapse at the mountain front  
598 of the northern Apennines (Italy), *Tectonics*, 31(4), 2012.

599 Toussaint, R., Aharonov, E., Koehn, D., Gratier, J. P., Ebner, M., Baud, P., Rolland, A., Renard, F.:  
600 Stylolites: A review, *Journal of Structural Geology*, 114, 163-195, 2018.

601 Varga, R.J.: Rocky Mountain foreland uplifts: products of a rotating stress field or strain partitioning?  
602 *Geology*, 21, 1115-1118, 1993.

603 Vermeesch, P.: Unifying the U–Pb and Th–Pb methods: joint isochron regression and common Pb  
604 correction, *Geochronology*, 2, 119-131, 2020.

605 Vidal-Royo, O., Koyi, H. A., & Muñoz, J.A.: Formation of orogen-perpendicular thrusts due to  
606 mechanical contrasts in the basal décollement in the Central External Sierras (Southern Pyrenees,  
607 Spain), *Journal of Structural Geology*, 31(5), 523-539, 2009.

608 Weil, A.B., Yonkee, W.A.: Layer-parallel shortening across the Sevier fold-thrust belt and Laramide  
609 foreland of Wyoming: spatial and temporal evolution of a complex geodynamic system, *Earth and  
610 Planetary Science Letters*, 357-358, 405-420, 2012.

611 Yamato, P., Kaus, B. J., Mouthereau, F., Castelltort, S.: Dynamic constraints on the crustal-scale rheology  
612 of the Zagros fold belt, Iran, *Geology*, 39, 815-818, 2011.

613 Wang Y., Zwingmann H., Zhou L., Lo C.-H., Viola G., Hao J.: Direct dating of folding events by  
614 <sup>40</sup>Ar/<sup>39</sup>Ar analysis of synkinematic muscovite from flexural-slip planes, *Journal of Structural Geology*,  
615 83, 46-59, 2016.

616

617 **Dataset availability:** Data either are available as supplementary material or come from properly cited  
618 literature.

619

620 **Author contribution:** Conceptualization : O. Lacombe, N. Beaudoin; Data acquisition : all authors;  
621 Visualization : O. Lacombe, N. Beaudoin, G. Hoareau, A. Labeur; Funding acquisition : N. Beaudoin;  
622 Writing – original draft preparation : O. Lacombe, N. Beaudoin; Writing – review and editing : O.  
623 Lacombe, N. Beaudoin, G. Hoareau, J.P. Callot

624

625 **Competing interest:** “The authors declare that they have no conflict of interest”

626

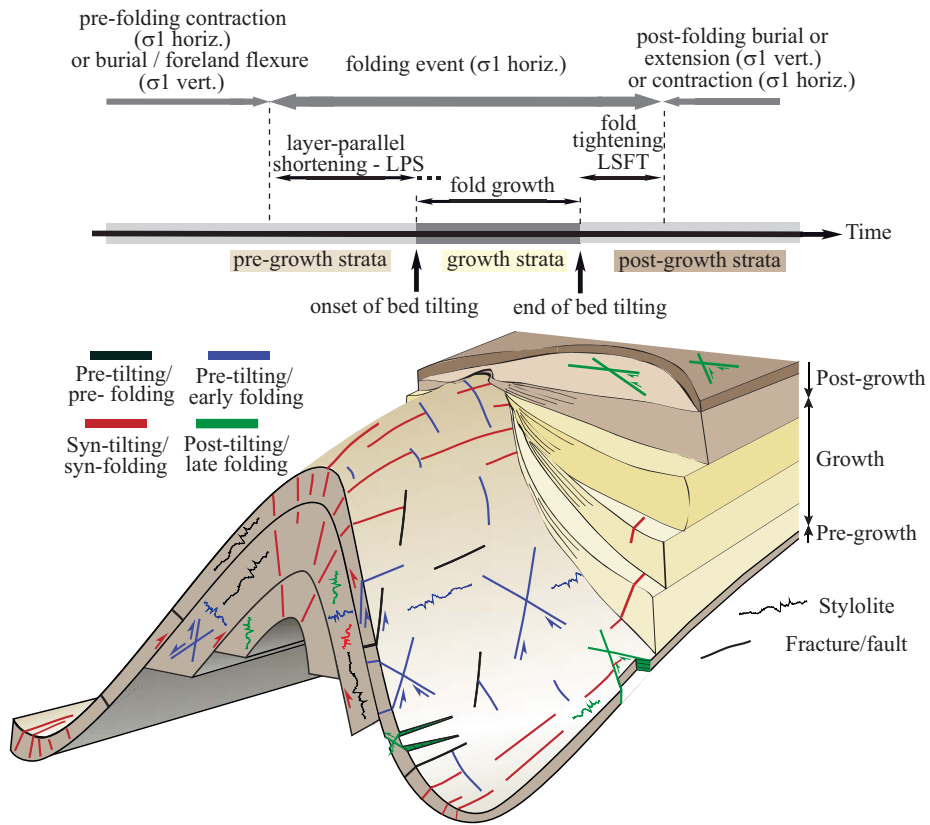


Fig.1. Concept of folding event and associated mesostructures and growth strata.

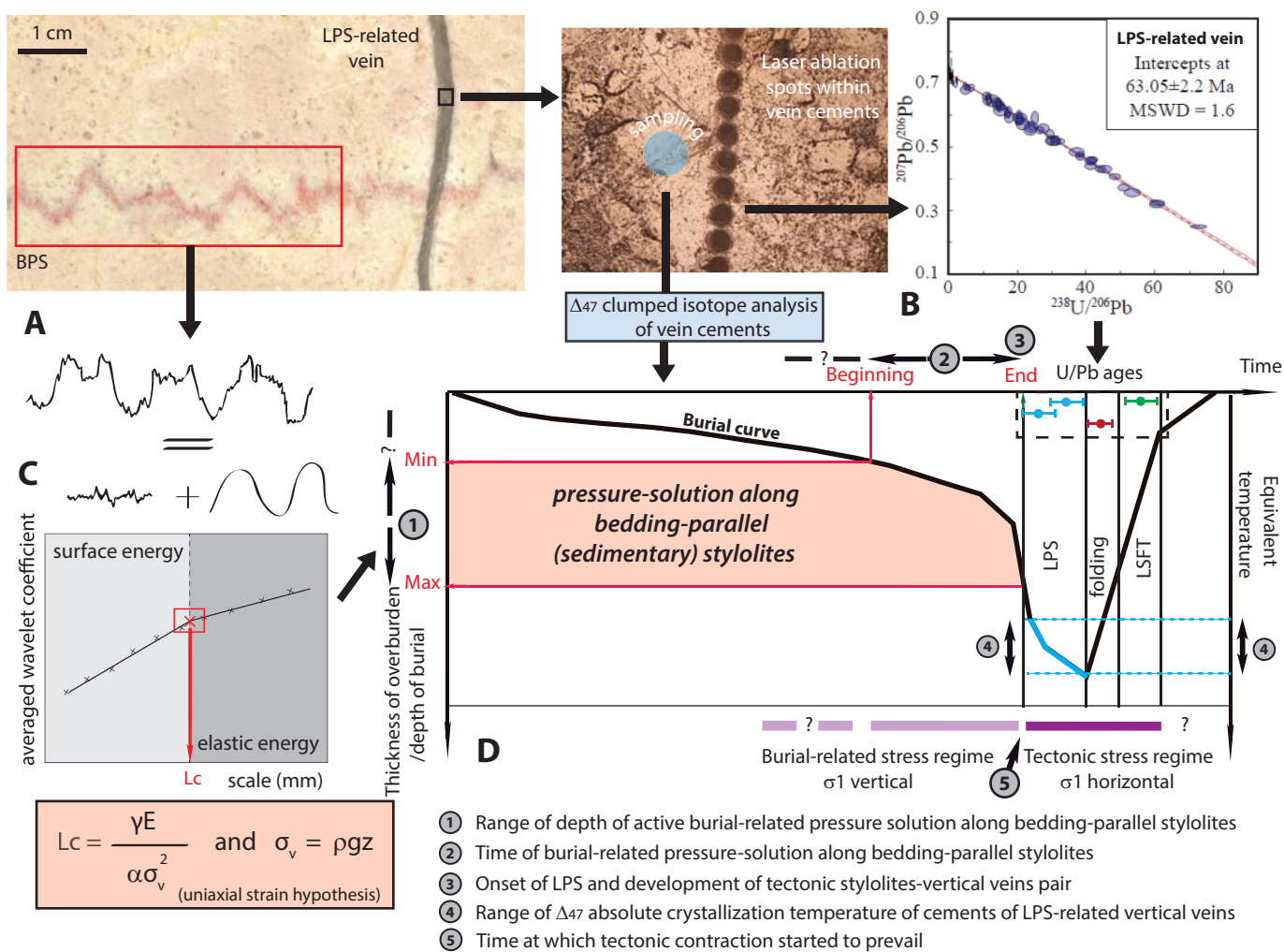


Fig.2. Principle of dating of mesostructures related to the folding event. A. Photograph of a sedimentary stylolite cut by a vertical vein related to layer-parallel shortening (LPS). B. Principle of dating calcite veins using LA-ICP-MS, with laser ablation spots and final Tera-Wasserburg diagram. C. Principle of inversion of the roughness of sedimentary stylolites for stress.  $\sigma_v$  is the vertical stress,  $\alpha = \frac{(1-2\nu)(1+\nu)^2}{30\pi(1-\nu)^2}$ ,  $\gamma$  is the solid-fluid interfacial energy,  $\nu$  is the Poisson ratio,  $E$  is the Young modulus,  $\rho$  is the dry density,  $g$  is the gravitational field acceleration and  $z$  is the depth. D. Principle of the combination of U-Pb dating and absolute  $\Delta 47$  thermometry of calcite cements (here for LPS-related veins) with maximum depth of burial-related dissolution from sedimentary stylolites and burial-time evolution of strata to derive the timing of deformation stages during the folding event.

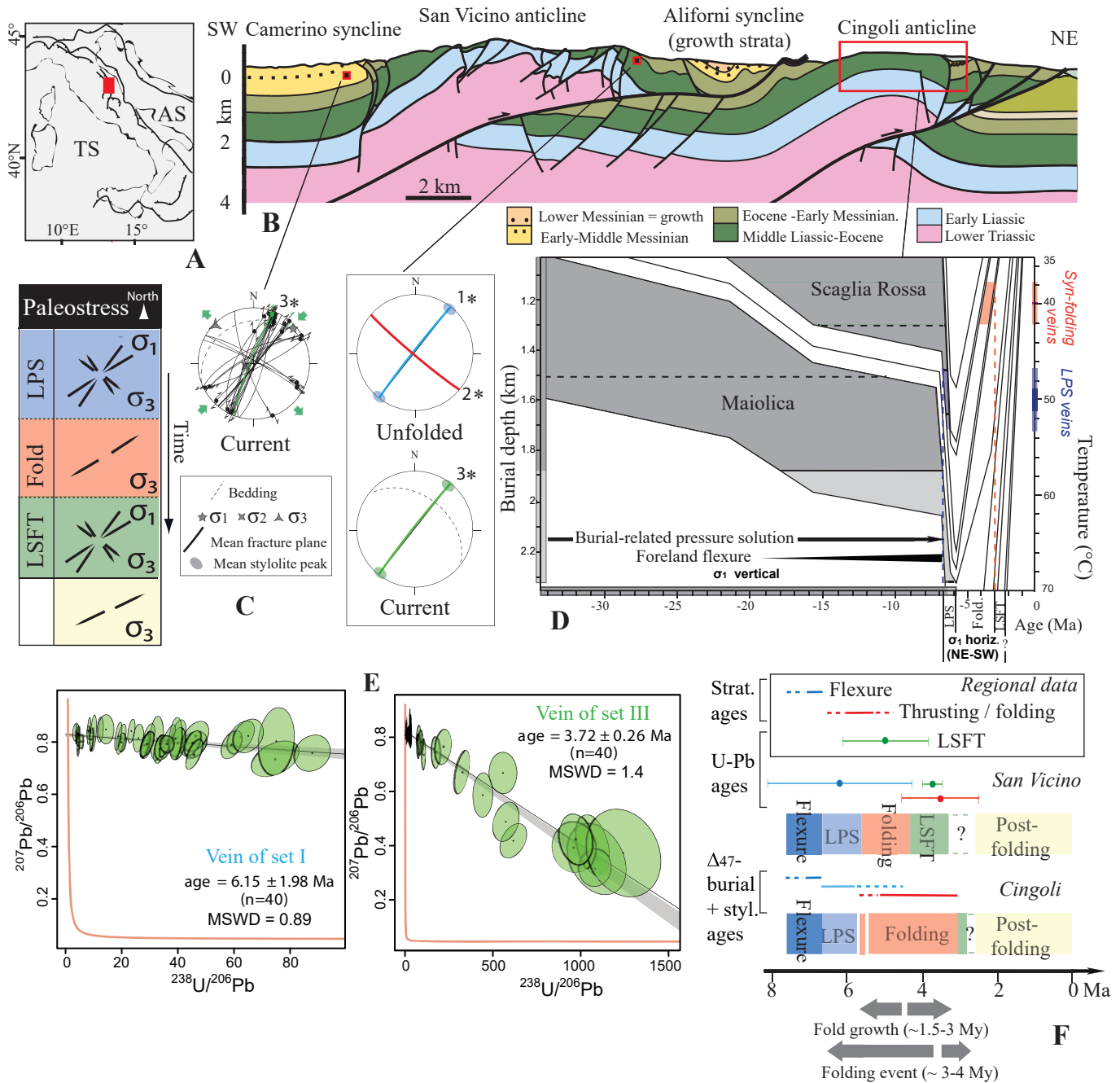


Fig.3. San Vicino and Cingoli anticlines: A: location (AS: Adriatic Sea; TS: Tyrrhenian Sea). B: Cross section (after Mazzoli et al., 2002). C: Orientation of the main sets of mesostructures (relative chronology, 1 to 3), reported in current or unfolded attitude on a lower hemisphere Schmidt stereonet, and associated paleostress evolution. \* denotes mesostructures dated using U-Pb. D: Burial model of Cingoli constructed considering thickness from stratigraphic and well data corrected for chemical and physical compaction (modified from Labeur et al., 2021). The range of depths reconstructed from sedimentary stylolite roughness inversion (with uncertainty shaded in light grey) are reported for each formation as grey levels. The results of clumped isotope analysis (i.e., temperatures of precipitation of vein cements at thermal equilibrium with the host rock) are reported for LPS-related veins (blue) and syn-folding veins (red). The deduced timing of the deformation stages is reported. E: Age dating results for veins from San Vicino anticline: Tera-Wasserburg concordia plots for carbonate samples showing  $^{238}\text{U}/^{206}\text{Pb}$  vs  $^{207}\text{Pb}/^{206}\text{Pb}$  for veins of sets I (LPS-related) and III (LSFT-related) (n—no. of spots). MSWD—mean square of weighted deviates. F: Timing and duration of deformation stages. Regional data are from Mazzoli et al., 2002 (flexure), Calamita et al. 1994 (folding and thrusting), Beaudoin et al., 2020c (LSFT). Color code for C and F: dark blue: flexure-related extension. blue: layer-parallel shortening (LPS); red: fold growth; green: late stage fold tightening (LSFT); yellow: post-folding extension.

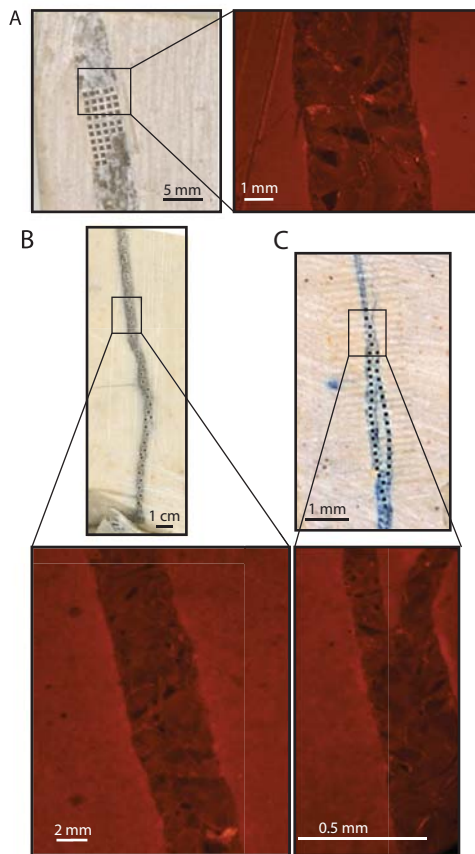


Fig.4. 2D scans of veins dated by LA-ICP-MS U-Pb geochronology from San Vicino anticline, with location of the ablation spots and diagenetic state observed under cathodoluminescence microscopy. A: sample A16 (LPS-related vein). B: sample A19 (syn-folding vein). C: sample A20 (LSFT-related vein).

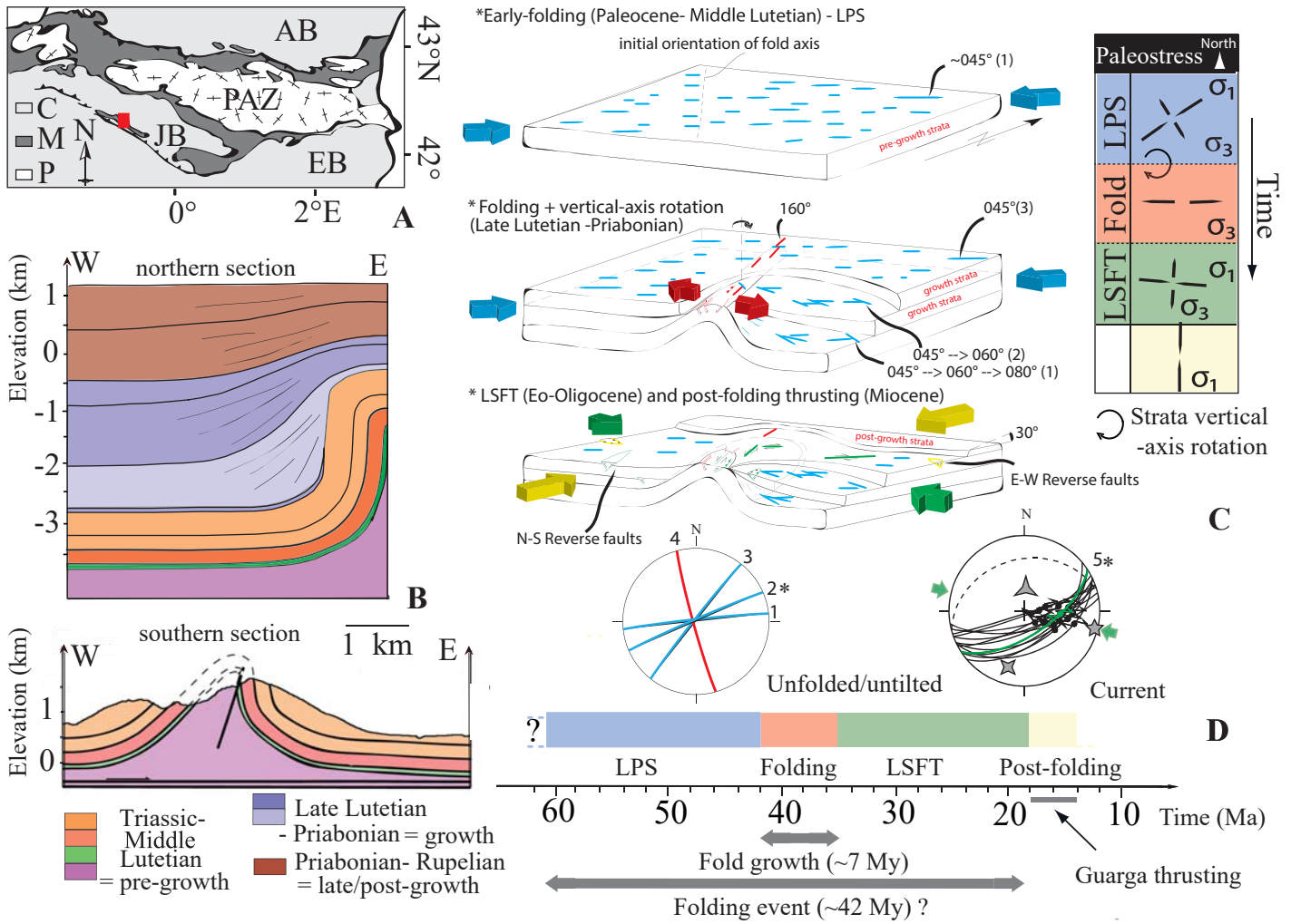


Fig.5. Pico del Aguila anticline: A: location (AB: Aquitaine Basin, JB: Jaca Basin, EB: Ebro Basin, PAZ: Pyrenean Axial Zone; P: Paleozoic; M: Mesozoic; C: Cenozoic). B: Cross sections (north after Poblet et al., 1997, south after Beaudoin et al., 2015). C: Orientation of the main sets of mesostructures (relative chronology, 1 to 5), reported in current or unfolded attitude on a lower hemisphere Schmidt stereonet (same key as Fig.3), and associated structural and paleostress evolution. Block diagrams modified after Beaudoin et al. (2015). \* denotes mesostructures dated using U-Pb. D : Timing and duration of deformation stages. Color code for C and D : blue: layer-parallel shortening (LPS); red: fold growth; green: late stage fold tightening (LSFT); yellow: post-folding compression.

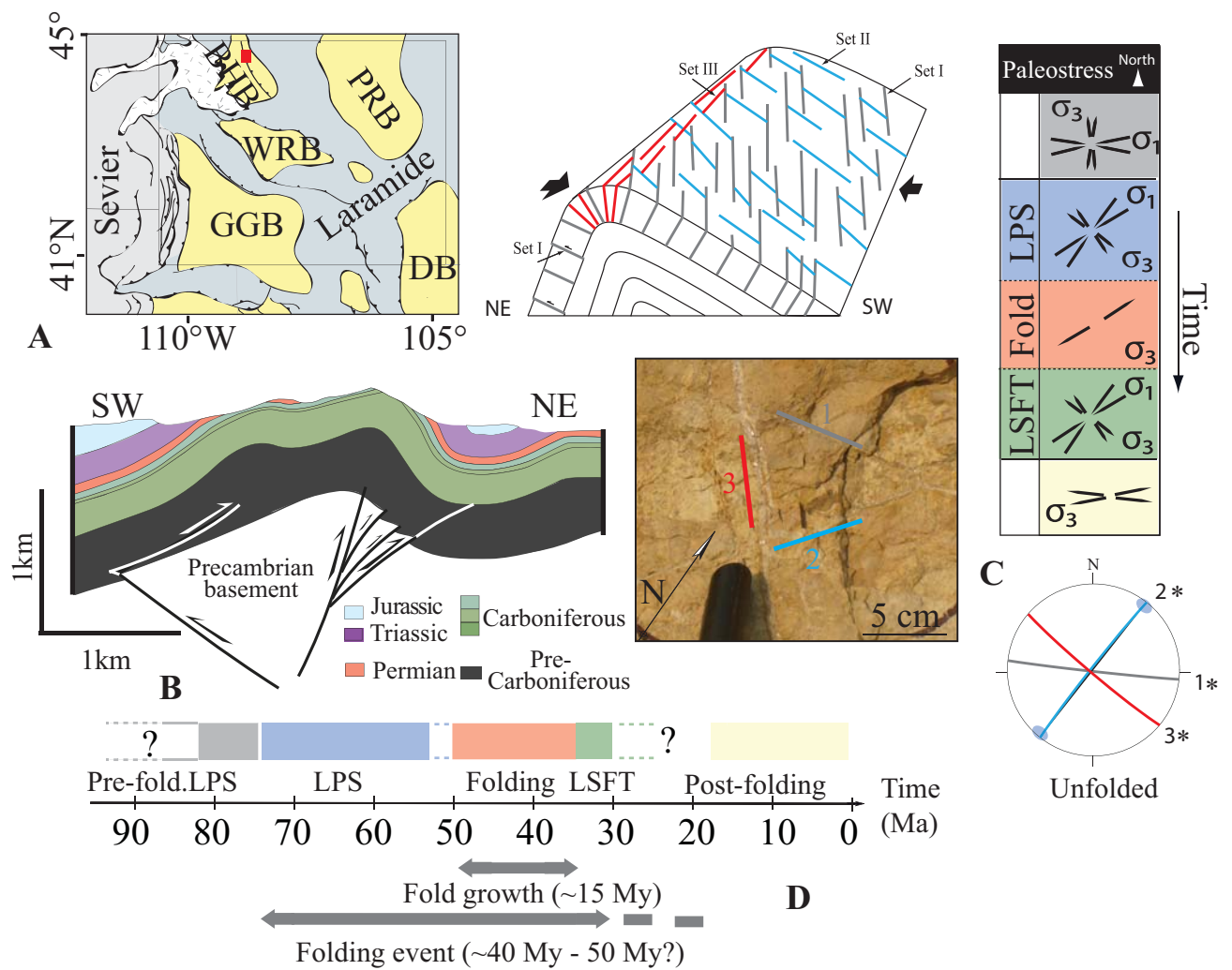


Fig.6. Sheep Mountain anticline: A: location (BHB: Bighorn Basin; WRB: Wind River Basin; PRB: Powder River Basin; GGB: Greater Green River Basin; DB: Denver Basin). B: Cross section (after Amrouch et al., 2010); C: Orientation of the main sets of veins (relative chronology, 1 to 3), shown on a field photograph and on a block-diagram of the final fold geometry, reported in unfolded attitude on a lower hemisphere Schmidt stereonet (same key as Fig.3), and associated structural and paleostress evolution. \* denotes mesostructures dated using U-Pb. D: Timing and duration of the deformation stages. Color code for C and D: grey: pre-folding layer-parallel shortening kinematically unrelated to folding; blue: layer-parallel shortening (LPS); red: fold growth; green: late stage fold tightening (LSFT); yellow: post-folding extension.

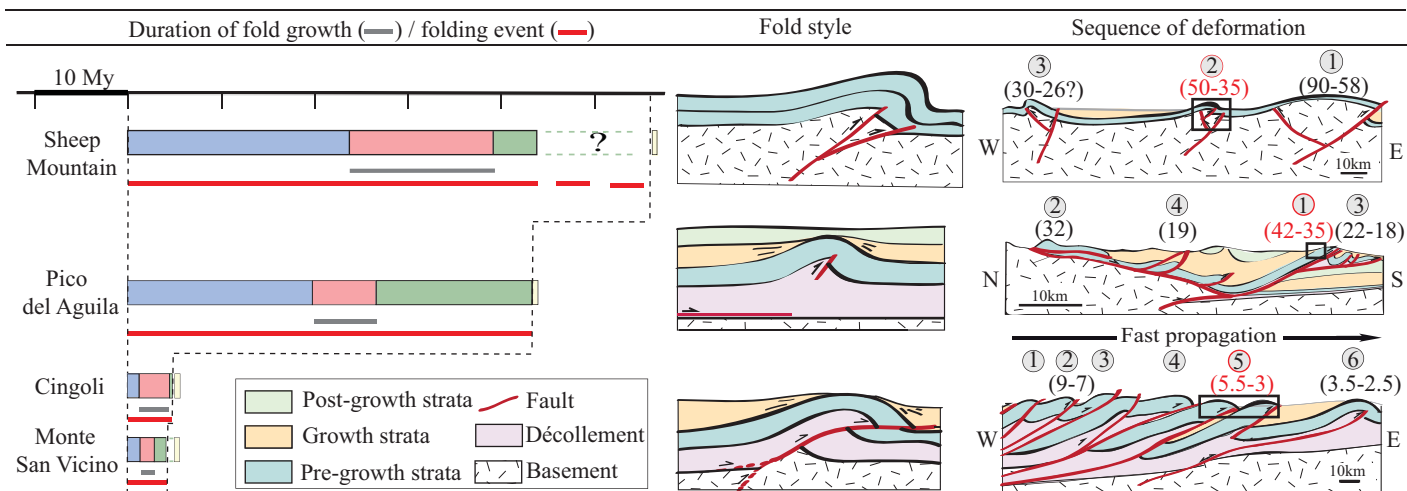


Fig.7. Compared durations of the stages of the folding event, fold style (= final fold geometry) and sequence of regional deformation for the four studied folds (circled numbers 1 to 6 : order of structural development, i.e., sequence of folding/thrusting, with corresponding ages in Ma (between parentheses), red : from this study; black : from the literature (Beaudoin et al., 2018 for Wyoming, Jolivet et al. 2007 for the Pyrenees, Calamita et al., 1994 and Curzi et al., 2020 for the Apennines). Color code: blue: layer-parallel shortening (LPS); red: fold growth; green: late stage fold tightening (LSFT); yellow: post-folding extension/compression.